Proceedings of the ASME 2024
18th International Conference on Energy Sustainability
ES2024
July 15-17, 2024, Anaheim, California

ES2024-131247

PROBING THERMAL TRANSPORT IN FLUIDIZED BED USING MODULATED PHOTOTHERMAL RADIOMETRY

Xintong Zhang[1], Sarath Reddy Adapa[1], Zhiwen Ma[2], Renkun Chen[1]

[1]Department of Mechanical and Aerospace Engineering, University of California, San Diego, La Jolla, California 92093, USA
[2]National Renewable Energy Laboratory, 15013 Denver W Pkwy, Golden, CO 80401, USA

ABSTRACT

In concentrated solar power (CSP) applications, fluidized bed is a promising approach for high heat transfer coefficient (HTC) solar receivers and heat exchangers. However, the complexity of multiphase mixing has made it difficult to characterize and analyze the heat transfer mechanism. This paper presents an experimental study on simultaneously characterizing heat transfer in both the near-wall and the bulk regions of a fluidized bed using modulated photothermal radiometry (MPR). The MPR is a non-contact frequency-domain technique using an intensity-modulated laser as the heat source and surface infrared emission as thermometry. The thermal penetration depth of the laser heating is varied by controlling its modulation frequency, and thus the measurement can resolve the near-wall and the bulk thermal resistances. With the MPR technique, we measured fluidized silica sands with a mean size of 164 μm in a vertical channel of 6 mm depth. Our results show that the near-wall thermal resistance is substantially increased with increasing gas velocity, which partially offsets the benefit of higher HTC brought by stronger particle mixing during the fluidization. We also used the MPR to quantify the improvement in particle-wall heat transfer in an inclined channel. We found that an 8° inclination towards the heat exchanging side led to a lower near-wall thermal resistance and a higher HTC at high gas velocities. This work demonstrates that the MPR technique is a useful tool to quantify the important near-wall thermal resistance from a bulk particle bed, which not only advances our understanding of heat transfer in fluidized beds, but may also contribute to the design of fluidized bed heat exchangers with higher HTC.

Keywords: Fluidized Bed, Photothermal Radiometry, Concentrated Solar Power, Heat Transfer Coefficient, Near-wall Thermal Resistance, Inclined Surface

NOMENCLATURE

Roman symbols

c	specific heat
D_{air}	thermal resistance as air gap thickness
D_p	mean particle size
e	thermal effusivity
f	frequency
k	thermal conductivity
h_w	particle-wall heat transfer coefficient
j	imaginary unit
L_p	thermal penetration depth
U_g	gas velocity
U_{mf}	minimum fluidization velocity
$\widetilde{U}$	dimensionless excess gas velocity

Greek symbols

α	thermal diffusivity
ε	emissivity
ρ	density
σ_{SB}	the Stefan-Boltzmann constant
θ_s	temperature oscillation amplitude
ω	angular frequency

Acronyms

CFD	computational fluid dynamics
CSP	concentrated solar power
DEM	discrete element method
HTC	heat transfer coefficient
MPR	modulated photothermal radiometry
OD	outside diameter of the gas distributor

1. INTRODUCTION

Fluidized beds have been widely used in various thermal processes due to their excellent heat and mass transfer characteristics, such as heat exchangers [1], thermochemical reactors [2], and combustors [3]. In the next-generation concentrated solar power (CSP) applications, fluidized bed receivers and heat exchangers can be operated at high temperatures (> 700 °C) to obtain high heat transfer coefficient (HTC) with certain particle materials and sizes [4]. Previous

experimental work has shown that the fluidized beds are capable to achieve particle-to-wall HTC (h_w) around 1,000 W m^{-2} K^{-1} at elevated temperatures and proper gas velocities (U_g) [5]. However, h_w of fluidized beds cannot be increased further at higher U_g despite the enhanced particle convection heat transfer in the bulk bed. It has been recognized that a non-negligible thermal resistance from fluidized particles to the wall lies in the near-wall region [6, 7], which hinders the further improvement of h_w. This near-wall thermal resistance was ascribed to a shorter particle-wall contact time (i.e., residence time on the wall) with stronger fluidization [8-10]. An effective air gap layer between the particle bed and the wall, representing the near-wall thermal resistance, was proposed to match experimental results and models [11-13]. The thickness of air gap (D_{air}) was estimated to be less than one single particle diameter [14]. Earlier studies relied on a series of thermocouples inserted into the fluidized bed to measure the temperature profile. Therefore, this thin air gap has never been directly quantified by conventional methods due to lower spatial resolution of the thermometry compared to the air gap thickness.

Efforts have been made to reduce the near-wall thermal resistance and enhance the overall h_w, such as tilting the heat exchanging surface. With the assistance of gravity, particles are expected to have better contact with an inclined surface. The h_w of a horizontal surface immersed in fluidized particles was found to be 10%-30% higher than that of a vertical surface [15]. It was also observed that the gas void fraction in the vicinity of an inclined plate placed in the fluidized bed could be modified by adjusting its angle of inclination [11]. Recently, a modeling work based on computational fluid dynamics (CFD) simulation illustrated a 34% increment in h_w after tilting the fluidized bed heat exchanger by only 5^o [16]. Nonetheless, there is still a lack of quantitative correlation between the angle of inclination and the near-wall thermal resistance.

Currently, the National Renewable Energy Laboratory (NREL) is developing a light-trapping, planar-cavity receiver (LTPCR) for high-temperature, high-performance applications in the Gen3 particle CSP and thermochemical processes. Particles are fluidized near the bottom of the receiver to improve the thermal transport between the wall and particles. By utilizing vertical planar cavities, the concentrated solar flux will spread and transform to low heat flux on receiver panel walls to accommodate relatively low heat transfer rate by solid particles. The test and optimization of the LTPCR system towards better performance will also benefit from a measurement technique that can simultaneously resolve the heat transfer in the near-wall and the bulk regions.

This work presents an experimental study on separately characterizing heat transfer in the near-wall and the bulk regions of a fluidized bed using modulated photothermal radiometry (MPR), which has been developed by us to measure the thermal transport properties of flowing liquids and moving particle beds in our previous studies [17, 18]. We measured fluidized silica sands with a mean size of 164 μm in a vertical 6 mm-deep channel at 300 ^{o}C. Our results show that the near-wall thermal resistance is increased by more than ten folds when the gas velocity changes from 0 to 42.0 cm s^{-1}, which partially offsets the benefit of stronger particle mixing and results in a maximum h_w around 500 W m^{-2} K^{-1}. We also found that an 8^o inclination towards the heat exchanging side led to a 36.1% reduction of the near-wall thermal resistance and a 28.0% increase in the overall h_w at high gas velocities. This work resolves the important near-wall thermal resistance of fluidized beds with different configurations in a unique way, which not only advances our understanding of heat transfer in fluidized beds, but may also contribute to a better design of fluidized bed heat exchangers with higher HTC.

2. METHODS

2.1 Fluidized Bed MPR Setup

A lab-scale fluidized bed test system was developed to study how the overall h_w and the near-wall thermal resistance vary with different fluidization conditions and channel configurations. As shown in **FIGURE 1**, the particle bed was confined in a rectangular Inconel 625 channel with bed depth of 6 mm and width of 30 mm. A 1/8 inch (OD) stainless steel tube was placed at the bottom of the channel as the gas distributor with five 0.8×0.4 mm rectangular holes uniformly distributed on it. The channel was sandwiched between two Inconel 625 plates, which had insertion heaters embedded in to heat up the fluidized bed to the desired test temperature. The air flow was controlled and monitored by a variable area flow meter with valve and a pressure gauge before injected into the particle bed. The fluidizing air was not pre-heated since it would be instantly heated up to the particle temperature in the flow rate range of this study. The hot air was exhausted to the ambient atmosphere through the opening at the top of the channel, which was covered by stainless steel wire cloth with a mesh size of 270 to filter particles. The entire channel was placed on an Inconel 625 base, which allowed the channel to have a maximum inclination angle of 8^o.

To apply the MPR technique, a 30×30 mm laser window is opened on the front Inconel plate, with its center located 4 cm above the gas distributor. As shown in **FIGURE 2**, the laser window was a piece of 100 μm-thick Inconel 625 shim sheet coated by 20 μm-thick Pyromark 2500 black paint for laser heat adsorption. The shim sheet side was in direct contact with the fluidized particles. A continuous wave laser beam with a top-hat profile and a diameter of 20 mm was shined on the Pyromark coating. The laser beam had its intensity modulated as a sinusoidal function at angular frequency ω ($\omega = 2\pi f$, f is the laser frequency) and it had a heat flux amplitude of q_s calibrated in the way introduced in our previous work [19]. The coating surface temperature will oscillate at amplitude $|\theta_s|$, which was collected by a high-temperature IR pyrometer (Lumasense Technologies IGA 320/23- LO). **FIGURE 2** shows that the diffusive thermal wave will travel and decay to a negligible level within a certain distance defined as the penetration depth (L_p):

$$L_p = \sqrt{\frac{\alpha}{\pi f}} \quad (1)$$

where $\alpha = k/\rho c$ is the thermal diffusivity of the sample, k is the thermal conductivity, ρ is the density, and c is the specific heat. By tuning the laser frequency, we were able to vary the thermal penetration depth in the fluidized bed thus probing the near-wall and the bulk regions separately. $|\theta_s|$ from MPR measurements was fitted by analytical models to extract the near-wall thermal resistance and the overall h_w, which will be demonstrated in detail later in this article.

Measurements were conducted with silica sands (Granusil W7020, Black Lab) with an average particle size D_p = 164 µm. The bulk material density of the sand is ρ_p = 2,650 kg m^{-3} and the specific heat is 1,050.8 J kg^{-1} K^{-1} at 300 °C [20]. The stationary W7020 bed before fluidization had a packing density of 57.7% and the minimum fluidization velocity (U_{mf}) was measured to be 4.2 cm s^{-1}.

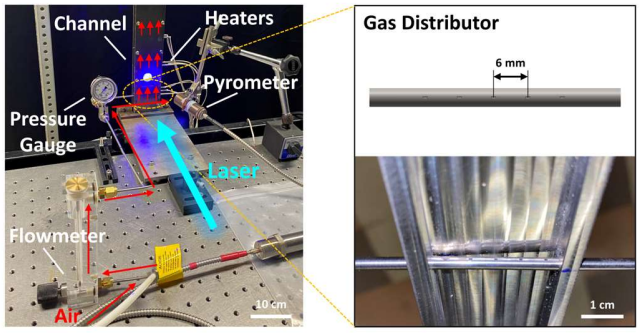

FIGURE 1: Photo of the fluidized bed system measured by MPR. Red arrows represent air flow.

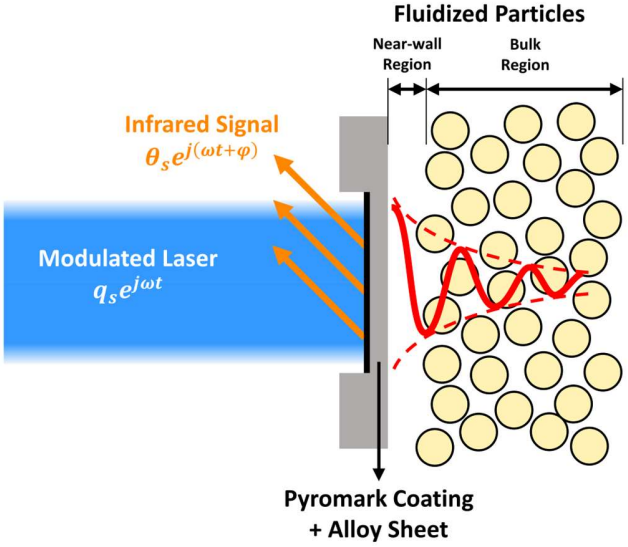

FIGURE 2: Schematic of MPR principle.

2.2 MPR Test Matrix

As shown in **Table 1**, fluidized beds under multiple conditions were measured by MPR at 300°C. Two different channel configurations were tested (**FIGURE 3**): fluidized bed in a vertical channel at U_g = 6.3, 16.0, 21.0, and 42.0 cm s^{-1}, and fluidized bed in an inclined channel towards the heat exchanging side with an angle of 8° at U_g = 16.0, 21.0, and 42.0 cm s^{-1}. Besides, MPR measurement on stationary W7020 bed without any fluidization was also conducted as a reference. Each test condition had at least 3 individual repeated measurements to minimize the error in the following model fitting process.

Table 1. Test matrix of fluidized W7020 beds.

Test	U_g (cm s^{-1})	Inclination (°)	Temperature (°C)
Stationary reference	0	0	300
Gas velocity sensitivity	6.3 - 42.0	0	300
Inclination sensitivity	16.0 - 42.0	8	300

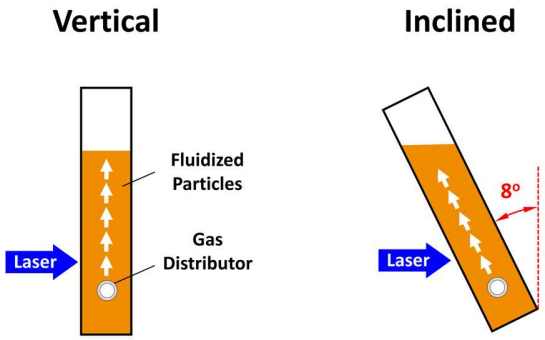

FIGURE 3: Side view of two channel configurations: vertical and 8° inclined. White arrows represent air flow.

2.3 MPR Analytical Models

The exact thermo-fluid transport of the fluidized particle bed is complex [21, 22] and its modeling is often computationally intensive [23]. To gain the insights of the heat transfer mechanisms without going through the complications of the exact modeling, we used two simplified models to fit the experimental data to obtain the overall particle-wall HTC (h_w) and near-wall air gap thickness (D_{air}). Both models are based on the analysis of a one dimensional (1-D) frequency-domain heat transfer problem [24].

2.3.1. Model with overall particle-wall HTC (h_w)

In this model, the heat transfer from the wall to the fluidized bed was treated as a convection boundary condition with an overall particle-wall HTC (h_w) and bed temperature T_∞ = 300

ºC. The geometry for the analytical model is shown below in **FIGURE 4**. The solid wall was divided into two layers corresponding to the experimental setup: layer 1 is the Pyromark coating with a thickness of 20 μm; layer 2 is the Inconel 625 shim sheet with a thickness of 100 μm; and the ambient air is denoted as layer 0. The sinusoidal laser heat flux with an amplitude q_s superimposed a periodic temperature field (T) throughout the domain.

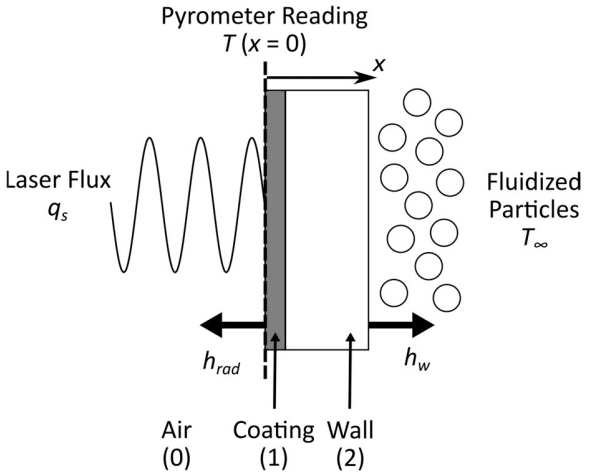

FIGURE 4: Geometry of the HTC model.

Since the pyrometer measures the surface temperature oscillation of the coating during the measurement, the equation was solved at position x = 0 and the amplitude (θ_s = T-T_∞) of the surface temperature oscillation is given as:

$$\theta_s(\omega) = \frac{q_s(1+R_1)}{2k_1\sigma_1}\left[\frac{1+\rho_{21}R_1e^{-2\sigma_1 D_1}}{1-\rho_{21}R_1e^{-2\sigma_1 D_1}}\right] \quad (2)$$

where

$$\rho_{21} = \frac{(1-b_{21}+R_T k_2\sigma_2)+R_2(1+b_{21})e^{-2\sigma_2 D_2}}{(1+b_{21}+R_T k_2\sigma_2)+R_2(1-b_{21})e^{-2\sigma_2 D_2}} \quad (3)$$

$$b_{21} = \frac{k_2\sigma_2}{k_1\sigma_1} \quad (4)$$

$$R_1 = \frac{k_1\sigma_1-k_0\sigma_0-h_{rad}}{k_1\sigma_1+k_0\sigma_0+h_{rad}} \quad (5)$$

$$R_2 = \frac{k_2\sigma_2-h_w}{k_2\sigma_2+h_w} \quad (6)$$

$$\sigma = (1+j)\sqrt{\frac{\omega}{2\alpha}} \quad (7)$$

The numbers in the subscript are layer indexes and D is the thickness of the corresponding layer. The radiation heat loss to the ambient from the high-emissivity coating was treated with the heat transfer coefficient h_{rad} below [25], where σ_{SB} is the Stefan-Boltzmann constant and ε is the coating emissivity measured to be 0.9 [26]:

$$h_{rad} = 4\varepsilon\sigma_{SB}T_\infty^3 \quad (8)$$

The overall h_w between the fluidized particles and the wall is the fitting parameter in this model. In **Section 3.1** and **3.2**, the h_w that best fits the MPR raw data under each test condition will be discussed in more detail. Conduction from the Pyromark coating to the ambient air and the contact thermal resistance between the coating and shim sheet $R_T = 1\times10^{-8}$ m^2 K W^{-1} were included for completeness of the model but their impact is negligible and can be safely ignored. Eqn. (2) was solved in MATLAB and fit to the experimental $|\theta_s| - \omega^{-1/2}$ curves using the least-squares minimization method implemented via the Trust-Region-Reflective algorithm. **FIGURE 5** shows the model fitting curves of raw data. In general, the analytical model has a good fitting quality and can well capture the trend of $|\theta_s|$ measured by MPR in the frequency domain, especially in the low frequency range where the thermal wave is long and well into the bulk fluidized bed region.

2.3.2. Model with near-wall air gap (D_{air})

One can see from **FIGURE 5** that there is a deviation between the model with h_w and the experimental data in the intermediate frequency range of $\omega^{-1/2}$ = 0.5-0.9 (corresponding to f = 0.20-0.64 Hz). According to penetration depth in the MPR experiment (Eqn. (1)), the measurement is more sensitive to the thermal resistance at the interface between the wall and the fluidized bed (i.e., the near-wall region) at this frequency. This deviation is caused by the simplification of using a single lumped parameter h_w to depict both the convection heat transfer in the bulk fluidized bed region and the near-wall conduction. If the near-wall thermal resistance is considered as an air gap, it has been estimated that the gap thickness (D_{air}) of 120 μm corundum particles fluidized by 250 ºC air is around 17 μm [11], or about 15% of the average particle size. The thermal conductance across this air gap is:

$$G_{air} = \frac{k_{air}}{D_{air}} \quad (9)$$

In our case, given k_{air} = 0.044 W m^{-1} K^{-1} at 300 ºC and D_{air} ~ 25 μm (~ 15% of D_p of W7020), G_{air} is about 1,800 W m^{-2} K^{-1}, which is much higher than the overall h_w (normally below 700 W m^{-2} K^{-1} at 300 ºC) between the fluidized bed and the wall. This explains the higher $|\theta_s|$ from the model with the single h_w parameter in the intermediate frequency range.

The data in this frequency range ($\omega^{-1/2}$ = 0.5-0.9) can be better fitted with the consideration of G_{air} to separately obtain the D_{air}. When $\omega^{-1/2}$ < 1, the impact of h_{rad} on θ_s can be neglected. With the bulk fluidized bed considered as a homogeneous phase with an effective thermal conductivity, the analytical solution of θ_s can be expressed as below instead of Eqn. (2):

$$\theta_s = \frac{\frac{e_3}{e_1}th_1th_3+\frac{e_2}{e_1}th_1th_2+\frac{e_3}{e_2}th_2th_3+1}{\frac{e_1}{e_3}th_1+\frac{e_1}{e_2}th_1th_2th_3+\frac{e_2}{e_3}th_2+th_3}\frac{q_s}{e_3\sqrt{j\omega}} \quad (10)$$

$$th_i = \tanh\left(\frac{D_i}{\sqrt{\alpha_i}}\sqrt{j\omega}\right) \quad (11)$$

where $e = \sqrt{\rho ck}$ is the thermal effusivity of each layer. Subscripts 1, 2, and 3 represent the Pyromark coated alloy sheet, the air gap, and the particle bed, respectively. When $\omega^{-1/2}$ = 0.5-0.9, the depth of fluidized bed is much greater than the penetration depth ($D_3 \gg L_p$), resulting in the term $th_3 \approx 1$. Therefore, Eqn. (10) can be simplified as:

$$\theta_s = \frac{\frac{e_3}{e_1}th_1+\frac{e_2}{e_1}th_1th_2+\frac{e_3}{e_2}th_2+1}{\frac{e_1}{e_3}th_1+\frac{e_1}{e_2}th_1th_2+\frac{e_2}{e_3}th_2+1}\frac{q_s}{e_3\sqrt{j\omega}} \quad (12)$$

Thus, D_{air} of the fluidized bed can be acquired by fitting $|\theta_s|$ in range of $\omega^{-1/2}$ = 0.5-0.9 with Eqn. (12).

3. RESULTS AND DISCUSSION

3.1 Heat Transfer in Vertical Fluidized Bed

The raw data from MPR measurements on fluidized beds in the vertical channel is shown in **FIGURE 5**. Qualitatively, a lower slope of curve in the $|\theta_s| - \omega^{-1/2}$ plot implies smaller local thermal resistance at that specific penetration depth. In the intermediate frequency range, the slope of raw data increases with the gas velocity, indicating a higher interfacial thermal resistance with stronger fluidization. At low frequency, the curves plateau at high gas velocity ($U_g \geq$ 16 cm/s) due to the strong convection heat transfer in the bulk region of the fluidized bed, a phenomenon we also observed in flowing fluids and moving particle beds in MPR experiments [18, 27].

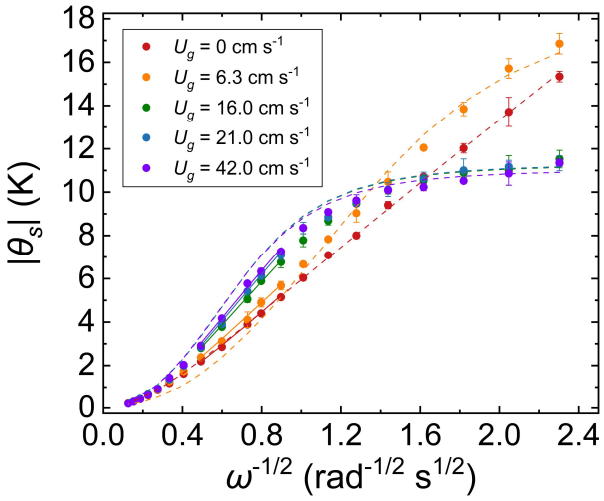

FIGURE 5: Raw data of MPR measurements on fluidized W7020 bed in vertical channel at 300 °C and various gas velocities. Dash line: HTC model fitting curves. Solid line: D_{air} model fitting curves.

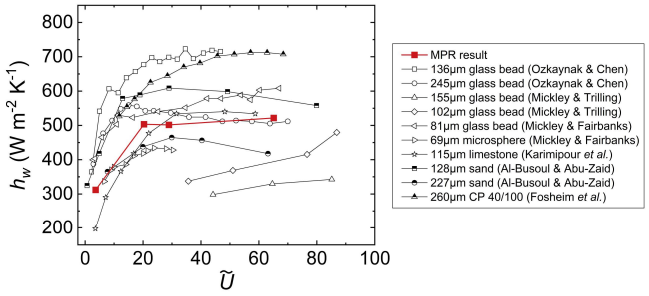

FIGURE 6: Fluidized bed overall HTC extracted from our MPR experiments and literature values of air fluidized beds below 350 °C.

FIGURE 6 shows the HTC model fitting results for fluidized bed in the vertical channel. A dimensionless excess gas velocity was defined as the following [28]:

$$\tilde{U} = \left(U_g - U_{mf}\right)\left(\frac{\rho_p c_p}{k_{air} g}\right)^{1/3} \quad (13)$$

This dimensionless group represents the ratio of heat transfer due to particle migration and gas conduction. Near the minimum fluidization condition ($\tilde{U} \approx 0$), h_w is as low as 312 W m^{-2} K^{-1} due to the insufficient particle mixing. As U_g increases to $2.5U_{mf}$ ($\tilde{U} \approx 20$), h_w has its maximum value slightly above 500 W m^{-2} K^{-1}. This trend agrees well with literature values of h_w in fluidized beds below 350 °C with similar particle sizes [8, 29-33], most of which have their plateau occurred at 20<$\tilde{U}$<50. At higher gas velocity, the increasing trend of h_w stops despite stronger bubbling in the bulk region, which can be explained by larger D_{air} at higher gas velocity, as discussed in **Section 3.3**.

3.2 Heat Transfer in Inclined Fluidized Bed

FIGURE 7 shows the MPR raw data from fluidized beds in the inclined channel. There is a clear difference in the MPR data between the inclined and vertical channels in the intermediate and low frequency ranges, implying the inclination changes both the near-wall thermal resistance and the overall h_w. The dash lines from the model with h_w agrees well with the raw data, especially at low frequency. The extracted h_w from the inclined channel is compared with that from the vertical channel, as shown in **FIGURE 8**. There is a considerable increase in h_w with the inclination at the high gas velocity. For example, it increases from 522 W m^{-2} K^{-1} to 668 W m^{-2} K^{-1} at U_g = 42.0 cm s^{-1}. However, this benefit from inclination is not evident at U_g = 16.0 cm s^{-1} A potential reason could be the deflection of the hot air flow towards the other side of the channel by the non-negligible buoyancy effect at low gas velocity. Consequently, a de-fluidized layer may form on the surface of the heat exchanging side [11], which could weaken the heat transfer in the bulk fluidized bed region. In previous experiments [15], it

was observed that the influence of inclining the heating surface on h_w is not clear for larger particles, which are more difficult to be fluidized. These facts may point to the same conclusion that a considerable enhancement of overall h_w can only be achieved by inclining the fluidized bed under strong fluidization conditions, for example, with high gas velocity or small particle size.

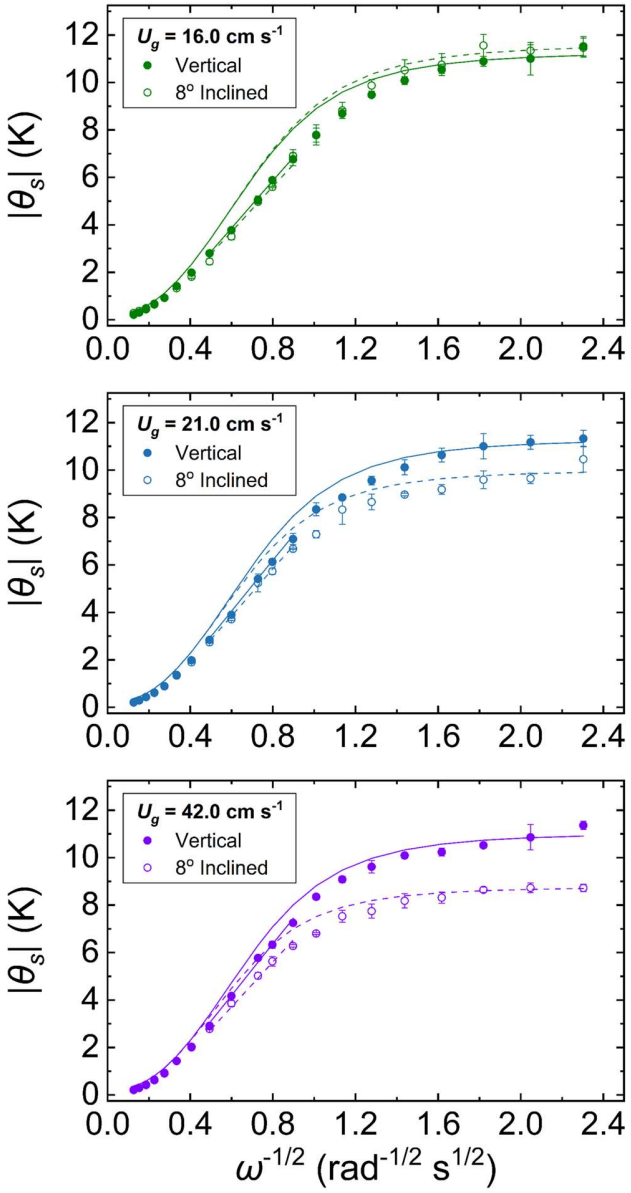

FIGURE 7: Raw data of MPR measurements on fluidized W7020 bed in inclined channel at 300 ºC and various gas velocities, compared with data from vertical channel. Solid line: model fitting curves of vertical channel data. Dash line: model fitting curves of inclined channel data.

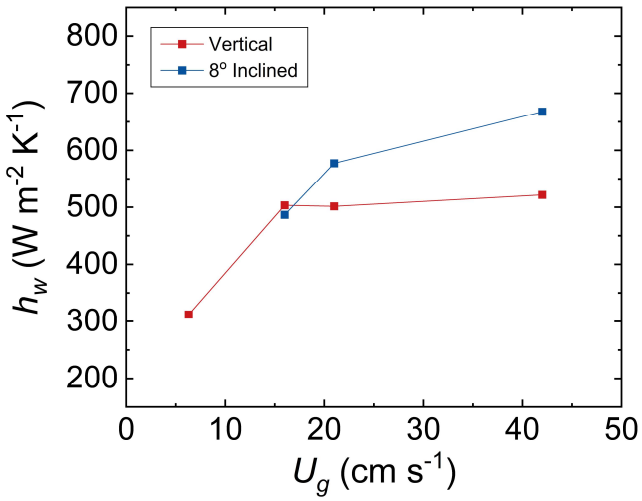

FIGURE 8: HTC of fluidized beds in vertical and inclined channels measured by MPR.

3.3 Air Gap of Vertical and Inclined Fluidized Beds

As discussed earlier, the MPR experiment can separately extract D_{air} in the intermediate frequency range. The modeled $|\theta_s| - \omega^{-1/2}$ curves with D_{air} as the fitting parameter using Eqn. (12) are shown as the solid lines in **FIGURE 5** and **FIGURE 7** for vertical and inclined fluidized beds respectively. **FIGURE 9** shows the extracted D_{air} values from the fitting.

The effective thermal conductivity k_{eff} and air gap thickness D_{air} of stationary W7020 bed without fluidization was measured as a reference using the MPR technique with the protocol described earlier [18]. At 300 ºC, the stationary W7020 bed has a k_{eff} = 0.30 W m^{-1} K^{-1} and an air gap thickness D_{air} = 4.1 μm. Compared to spherical CARBO ceramic particles (D_p = 275 and 404 μm) with D_{air} = 15-20 μm [18], the relatively small D_{air} of W7020 results from its smaller particle size as well as the irregular particle shape, which leads to lower porosity in the near-wall region.

For fluidized beds in the vertical channel, the D_{air} increases from 4.1 μm to 48.7 μm as the gas velocity increases from 0 cm s^{-1} to 42.0 cm s^{-1}, which is much higher than the typical air gap thickness of around $1/10 \times D_p$ in moving particle beds [18, 34]. This significant tenfold increment in the near-wall thermal resistance can be attributed to less particle clusters in contact with the wall and shorter particle residence time on the wall [8, 9], which obstructs the further increase of h_w at high gas velocity. Compared to the fluidization in the vertical channel, an 8º inclination towards the heat exchanging side helps to decrease the D_{air} by 6.2-17.6 μm, which equals to a 16.6%-36.1% reduction in the near-wall thermal resistance. With the assistance of gravity, fluidized particles gain a better contact with the surface, leading to a substantially higher overall h_w.

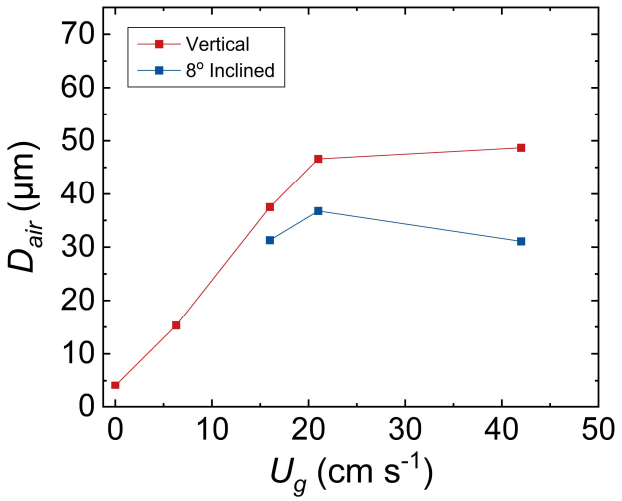

FIGURE 9: Near-wall thermal resistance as air gap thickness of fluidized beds in vertical and inclined channels measured by MPR.

3.4 Discussion

With the development of two analytical models, the near-wall thermal resistance and the overall h_w are successfully extracted from the MPR raw data of fluidized beds. The findings clearly show how the heat transfer between fluidized particles and the wall evolves with the gas velocity. However, there still exist limitations in the current work. As discussed previously, the model with h_w lacks a refined depiction in the near-wall region of fluidized beds. Meanwhile, the accuracy of the model with D_{air} relies on an appropriate estimation of the time-averaged effusivity of the bulk fluidized bed, which may benefit from proper discrete element method (DEM) simulations. To better predict D_{air} and h_w from MPR measurements, a more delicate analytical MPR model combining both the near-wall thermal resistance and the particle-to-wall HTC is preferred.

Besides, this work sheds a light on the mitigation of the near-wall thermal resistance and the improvement of the overall HTC in fluidized beds. Although the parameter space studied here is limited, a new methodology has been proved feasible for future experimental studies. By using the MPR technique to measure fluidized beds with various particle sizes, channel depths, inclination angles, gas distributor geometries, a complete picture of heat transfer in fluidized beds can be presented to the community.

4. CONCLUSION

The work presented in this paper demonstrates a unique frequency-domain technique (MPR) to probe the heat transfer process between particles and the wall in a fluidized bed. The near-wall thermal resistance and the overall particle-to-wall HTC were separately characterized by the MPR. For W7020 silica sands fluidized by air in a vertical channel at 300 ºC, the overall HTC shows good agreement with literature values at various gas velocities. The near-wall thermal resistance increases significantly at stronger fluidization and it is equivalent to a 48.7 μm-thick air gap layer between particles and the wall at high gas velocity. Besides, an enhanced thermal transport was observed by MPR in an inclined fluidized bed. An 8º inclination towards the heat exchanging side results in a 28.0% increase in the overall HTC due to a 36.1% lower near-wall thermal resistance. This work exhibits that the MPR technique is a useful tool for understanding and optimizing the heat transfer in fluidized beds.

ACKNOWLEDGEMENTS

This material is based upon work supported by the U.S. Department of Energy's Office of Energy Efficiency and Renewable Energy (EERE) under the Solar Energy Technologies Office Award Number DE-EE0038896 (for fluidized bed development) and DE-EE0008379 & DE-EE0009825 (for MPR instrumentation). The authors also appreciate the valuable discussions with Dr. Xingchao Wang of Colorado School of Mines.

REFERENCES

[1] Wu, C., Yang, H., He, X., Hu, C., Yang, L., and Li, H., 2022, "Principle, development, application design and prospect of fluidized bed heat exchange technology: Comprehensive review," Renewable and Sustainable Energy Reviews, 157, 112023.

[2] Tregambi, C., Salatino, P., Solimene, R., and Montagnaro, F., 2018, "An experimental characterization of Calcium Looping integrated with concentrated solar power," Chemical Engineering Journal, 331, pp. 794-802.

[3] Koornneef, J., Junginger, M., and Faaij, A., 2007, "Development of fluidized bed combustion—An overview of trends, performance and cost," Progress in energy and combustion science, 33(1), pp. 19-55.

[4] Mehos, M., Turchi, C., Vidal, J., Wagner, M., Ma, Z., Ho, C., Kolb, W., Andraka, C., and Kruizenga, A., 2017, "Concentrating solar power Gen3 demonstration roadmap," National Renewable Energy Lab.(NREL), Golden, CO (United States).

[5] Miller, D. C., Pfutzner, C. J., and Jackson, G. S., 2018, "Heat transfer in counterflow fluidized bed of oxide particles for thermal energy storage," International Journal of Heat and Mass Transfer, 126, pp. 730-745.

[6] Ma, Z., and Martinek, J., "Fluidized-bed heat transfer modeling for the development of particle/supercritical-CO2 heat exchanger," Proc. Energy Sustainability 2017, V001T05A002, American Society of Mechanical Engineers.

[7] Gloski, D., Glicksman, L., and Decker, N., 1984, "Thermal resistance at a surface in contact with fluidized bed particles," International journal of heat and mass transfer, 27(4), pp. 599-610.

[8] Karimipour, S., Zarghami, R., Mostoufi, N., and Sotudeh-Gharebagh, R., 2007, "Evaluation of heat transfer coefficient in gas–solid fluidized beds using cluster-based approach," Powder technology, 172(1), pp. 19-26.

[9] Zarghami, R., Mostoufi, N., Sotudeh-Gharebagh, R., and Chaouki, J., 2007, "Analysis and modeling of particle–wall

contact time in gas fluidized beds," Chemical engineering science, 62(17), pp. 4573-4578.
[10] Ambler, P., Milne, B., Berruti, F., and Scott, D., 1990, "Residence time distribution of solids in a circulating fluidized bed: Experimental and modelling studies," Chemical Engineering Science, 45(8), pp. 2179-2186.
[11] Baskakov, A. u., Berg, B., Vitt, O., Filippovsky, N., Kirakosyan, V., Goldobin, J., and Maskaev, V., 1973, "Heat transfer to objects immersed in fluidized beds," Powder Technology, 8(5-6), pp. 273-282.
[12] Botterill, J. S. M., 1970, "Heat transfer to gas-fluidized beds," Powder Technology, 4(1), pp. 19-26.
[13] Donsí, G., and Ferrari, G., 1995, "Heat transfer coefficients between gas fluidized beds and immersed spheres: dependence on the sphere size," Powder technology, 82(3), pp. 293-299.
[14] Patil, D., Smit, J., van Sint Annaland, M., and Kuipers, J., 2006, "Wall-to-bed heat transfer in gas–solid bubbling fluidized beds," AIChE Journal, 52(1), pp. 58-74.
[15] Stojanovic, B., Janevski, J., and Stojiljkovic, M., 2009, "Experimental investigation of thermal conductivity coefficient and heat exchange between fluidized bed and inclined exchange surface," Brazilian Journal of Chemical Engineering, 26, pp. 343-352.
[16] Appaswamy, K., Schirck, J., Punchi Wedikkara, C., Morris, A., and Ma, Z., "Multiphase Modeling in a Parallel Plate Fluidized Bed Receiver for Concentrating Solar Power," Proc. Energy Sustainability 2023, V001T05A001, American Society of Mechanical Engineers.
[17] Zeng, J., Chung, K. M., Adapa, S. R., Feng, T., and Chen, R., 2021, "In-situ thermal transport measurement of flowing fluid using modulated photothermal radiometry," International Journal of Heat and Mass Transfer, 180, 121767.
[18] Zhang, X., Adapa, S., Feng, T., Zeng, J., Chung, K. M., Ho, C., Albrecht, K., and Chen, R., 2023, "Micromechanical Origin of Heat Transfer to Granular Flow," arXiv preprint arXiv:2311.11244.
[19] Zeng, J., Chung, K. M., Wang, Q., Wang, X., Pei, Y., Li, P., and Chen, R., 2021, "Measurement of high-temperature thermophysical properties of bulk and coatings using modulated photothermal radiometry," International Journal of Heat and Mass Transfer, 170, 120989.
[20] Baumann, T., and Zunft, S., 2015, "Properties of granular materials as heat transfer and storage medium in CSP application," Solar Energy Materials and Solar Cells, 143, pp. 38-47.
[21] Saxena, S., Grewal, N., Gabor, J., Zabrodsky, S., and Galershtein, D., 1979, "Heat transfer between a gas fluidized bed and immersed tubes," Advances in Heat Transfer, 14, pp. 149-247.
[22] Gutfinger, C., and Abuaf, N., 1974, "Heat transfer in fluidized beds," Advances in heat transfer, Elsevier, pp. 167-218.
[23] Ostermeier, P., DeYoung, S., Vandersickel, A., Gleis, S., and Spliethoff, H., 2019, "Comprehensive investigation and comparison of TFM, DenseDPM and CFD-DEM for dense fluidized beds," Chemical Engineering Science, 196, pp. 291-309.
[24] Mandelis, A., 2001, "Thermal-wave fields in one dimension," Diffusion-Wave Fields: Mathematical Methods and Green Functions, Springer, pp. 85-166.
[25] Chung, K. M., Feng, T., Zeng, J., Adapa, S. R., Zhang, X., Zhao, A. Z., Zhang, Y., Li, P., Zhao, Y., and Garay, J. E., 2023, "Thermal conductivity measurement using modulated photothermal radiometry for nitrate and chloride molten salts," International Journal of Heat and Mass Transfer, 217, 124652.
[26] Rubin, E. B., Chen, Y., and Chen, R., 2019, "Optical properties and thermal stability of Cu spinel oxide nanoparticle solar absorber coatings," Solar energy materials and solar cells, 195, pp. 81-88.
[27] Chung, K. M., Zhang, Y., Zeng, J., Haddad, F., Adapa, S., Feng, T., Li, P., and Chen, R., 2023, "In-situ thermophysical measurement of flowing molten chloride salt using modulated photothermal radiometry," Solar Energy, 265, 112124.
[28] Molerus, O., 1992, "Heat transfer in gas fluidized beds part 2. Dependence of heat transfer on gas velocity," Powder technology, 70(1), pp. 15-20.
[29] Ozkaynak, T. F., and Chen, J. C., 1980, "Emulsion phase residence time and its use in heat transfer models in fluidized beds," AIChE Journal, 26(4), pp. 544-550.
[30] Mickley, H. S., and Trilling, C. A., 1949, "Heat transfer characteristics of fluidized beds," Industrial & Engineering Chemistry, 41(6), pp. 1135-1147.
[31] Mickley, H., and Fairbanks, D. F., 1955, "Mechanism of heat transfer to fluidized beds," AIChE Journal, 1(3), pp. 374-384.
[32] Al-Busoul, M., and Abu-Zaid, M., 2000, "Prediction of heat transfer coefficient between immersed surfaces and fluidized beds," International communications in heat and mass transfer, 27(4), pp. 549-558.
[33] Fosheim, J. R., Hernandez, X., Abraham, J., Thompson, A., Jesteadt, B., and Jackson, G. S., "Narrow-channel fluidized beds for particle-sCO2 heat exchangers in next generation CPS plants," Proc. AIP Conference Proceedings 2022, 2445, 1, AIP Publishing.
[34] Sullivan, W. N., and Sabersky, R., 1975, "Heat transfer to flowing granular media," International Journal of Heat and Mass Transfer, 18(1), pp. 97-107.

